

## ARTICLE OPEN



# Water stable and matrix addressable OLED fiber textiles for wearable displays with large emission area

Hayoung Song<sup>1,3</sup>, Young Jin Song<sup>1,3</sup>, Jinwook Hong<sup>1</sup>, Ki Suk Kang<sup>2</sup>, Sera Yu<sup>1</sup>, Ha-Eun Cho<sup>1</sup>, Jae-Hun Kim<sup>1</sup> and Sung-Min Lee<sup>1</sup>✉

Organic light-emitting diode (OLED) fibers with favorable electroluminescence properties and interconnectable pixel configurations have represented the potential for wearable electronic textile displays. Nevertheless, the current technology of OLED fiber-based textile displays still leaves to be desired due to several challenges, including limited emission area and lack of encapsulation systems. Here we present a fibrous OLED textile display that can attain a large emission area and long-term stability by implementing addressable networks comprised of integrated phosphorescence OLED fibers and by designing multilayer encapsulations. The integrated fiber configuration offers decoupled functional fiber surfaces for an interconnectable 1-dimensional OLED pixel array and a data-addressing conductor. Tailored triadic metal/ultrathin oxide/polymer multilayer enables not only the oxygen/water permeation inhibition but also the controllable conductive channels of dielectric antifuses. Together with reliable bending stability, the long-term operation of OLED textiles in water manifests the feasibility of the present device concept toward water-resistant full-emitting-area fibrous textile displays.

npj Flexible Electronics (2022)6:66; <https://doi.org/10.1038/s41528-022-00199-z>

## INTRODUCTION

Wearable electronic textiles (e-textiles) have been of great interest owing to their many compelling applications, such as healthcare monitoring/therapy systems, portable energy harvesting devices, and functional outdoor clothes/accessories<sup>1–4</sup>. One alluring format of e-textile devices is the e-textile displays that can visually deliver communication information and also provide a high degree of aesthetic design freedom<sup>5–8</sup>. As a fundamental building block for such e-textile displays, self-emissive lighting fibers were demonstrated at the early stage by exploiting various existing flexible lighting technologies, including electroluminescent units<sup>8–10</sup>, electrochemical cells<sup>11,12</sup>, electrochromic devices<sup>13,14</sup>, and light-emitting diodes<sup>15–21</sup>. Among these various lighting fibers, organic light-emitting diode (OLED) fibers have shown impressive progress by achieving high-class electroluminescence (EL) performance with low operating voltages<sup>19–22</sup>. Over the simple formation of planar OLEDs on textile substrates<sup>23–25</sup>, OLED fiber configurations could be created through vacuum<sup>19</sup> or solution<sup>20–22</sup> processes available with one-dimensional fiber substrates. In particular, with fiber-to-fiber interconnectable pixel configurations (i.e., separately defined outer pixel contacts), 2-dimensional matrix interconnections for the pixel addressing have been attained from instant contacts between the perpendicularly interlaced OLED fibers and conductive addressing fibers<sup>19,21</sup>, leading to actual display textiles over lighting textiles.

Despite the technical advances, the current level of OLED fiber technology is still rather in the immature stage due to challenging hurdles. For instance, a portion of the non-emitting area over the available textile area is considerably large due to the nature of interlacing networks in which OLED emitting fibers are alternately obscured by orthogonally placed non-emitting addressing fibers<sup>19,21</sup>. This results in limited resolution and, therefore, image quality. In addition, the well-developed thin-film encapsulations (TFEs) with hardly-patternable dense

dielectric (e.g., metal oxide) barriers<sup>26–31</sup> formed by atomic layer deposition (ALD) or chemical vapor deposition (CVD) cannot be directly applied to the interconnectable OLED fibers due to the concern of the pixel contact off arising from insulating the exposed pixel contact pads. The lack of high-grade barrier encapsulations is a critical challenge to reaching a practically applicable level of e-textile OLED displays in consideration of their serious vulnerability to the permeation of oxygen or moisture.

To address these issues of the emission area reduction by non-emitting fibers and the underdeveloped encapsulation systems for interconnectable OLED fibers, here we suggest strategic solution options for large emitting-area, highly durable OLED textile displays by applying (i) the addressable network only with integrated OLED emitting fibers and (ii) tailored TFE designs to interconnectable fiber configurations. To enable the matrix addressability without non-emitting addressing fibers, a phosphorescent OLED pixel array is assembled on a half-side of a rectangular strip fiber, while an independent conductor is formed on the opposite fiber side for supplying the electrical power to OLED pixels of interlaced fibers. Unlike the typical TFEs composed of oxide/polymer multilayer<sup>18,27–30</sup>, metal/ultrathin (~5 nm) oxide/polymer multilayer TFE is employed as a top encapsulation system for the OLED fiber pixels with exposed contact pads. This multilayer TFE features (i) high permeation barrier property that secures reliable OLED operations even in the water and (ii) controllable conductive domains that offer electrical circumventing paths between pixels and outer contact pads without the oxide patterning. Detailed device designs, fabrication processes, and experimental characterizations, together with proof-of-concept device demonstrations, systematically support the feasibility of the proposed approaches to full emitting-area water-resistant fibrous OLED e-textile displays.

<sup>1</sup>School of Materials Science and Engineering, Kookmin University, Seoul 02707, Republic of Korea. <sup>2</sup>School of Electrical Engineering, KAIST, Daejeon 34141, Republic of Korea.

<sup>3</sup>These authors contributed equally: Hayoung Song, Young Jin Song. ✉email: [sungminlee@kookmin.ac.kr](mailto:sungminlee@kookmin.ac.kr)

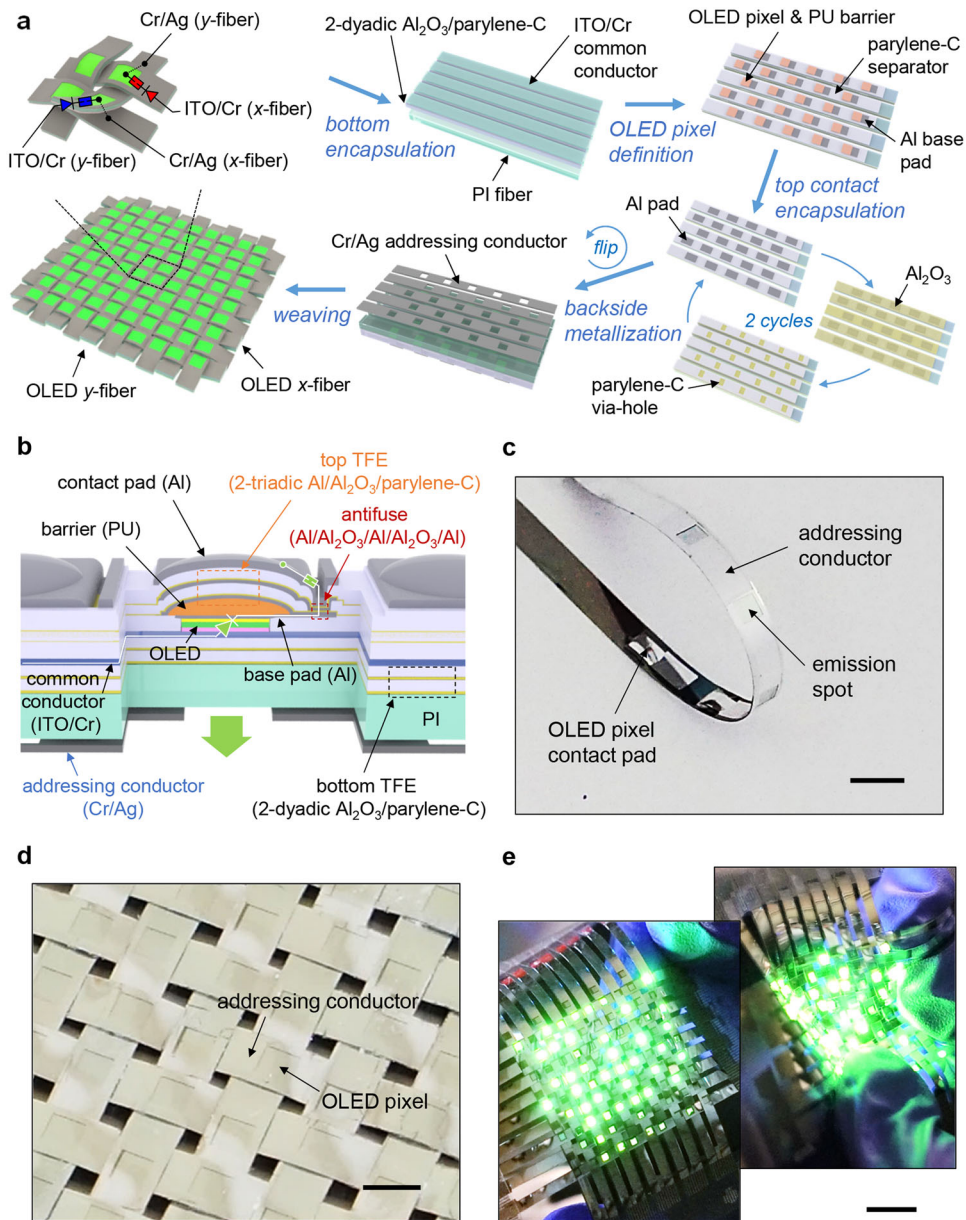


**Fig. 1 Design and fabrication of fibrous OLED textile displays with large emitting-area and long-term stability.** **a** Schematic illustration of the fabrication processes for a fibrous textile display consisting of encapsulated OLED fibers integrated with decoupled addressing conductors. **b** Cross-sectional illustration of an interconnectable OLED fiber pixel passivated with top and bottom TFEs. **c–e** Photographic images of fabricated single OLED fiber with 5 pixels **c** and woven textile device composed of  $10 \times 10$  OLED fiber arrays (**d**, **e**). Scale bars are 3 mm in **c**, 2 mm in **d**, and 1 cm in **e**, respectively.

## RESULTS

### Design and fabrication of encapsulated OLED fiber displays

Figure 1a, b schematically illustrate a proposed device design of OLED fiber display and its fabrication procedures. The device is created only with perpendicularly interlaced, encapsulated interconnectable OLED fibers integrated with data-addressing conductors. A half-side of a single OLED fiber consists of a 1-dimensional array of bottom-emission OLED pixels that share a common conductor connected to their anodes but possess individual contact pads linked to their own cathodes over the top encapsulation. On the other hand, the opposite half-side is utilized to span a separate electrical channel with an emission-aperture-defined conductor involved in the pixel addressing from instant contacts with OLED pixel pads on interlaced other fibers. Because every cross-spots of the woven network with these OLED fibers

implement physical contact between the OLED pixel pad and the orthogonal addressing conductor, they all can participate in the light emission, meaning that the light dead spots appearing in the previously reported woven textile displays with non-emitting conductive fibers<sup>17,19</sup> can be eliminated. The woven textile format with all emitting fibers is advantageous for increasing the emission area fraction against the available textile area compared to that with emitting/non-emitting fibers even at various fiber widths and gaps, which is discussed in detail in the Supplementary Information (Supplementary Notes, Supplementary Fig. 1–3).

The device fabrication began with the formation of the encapsulated OLED pixel arrays on fibers. Colorless polyimide (PI) strips with a rectangular cross-section ( $2 \times 0.15 \text{ mm}^2$ ) were used as base fibers due to their clear division definition (i.e., the OLED pixel array on the front side and the addressing conductor

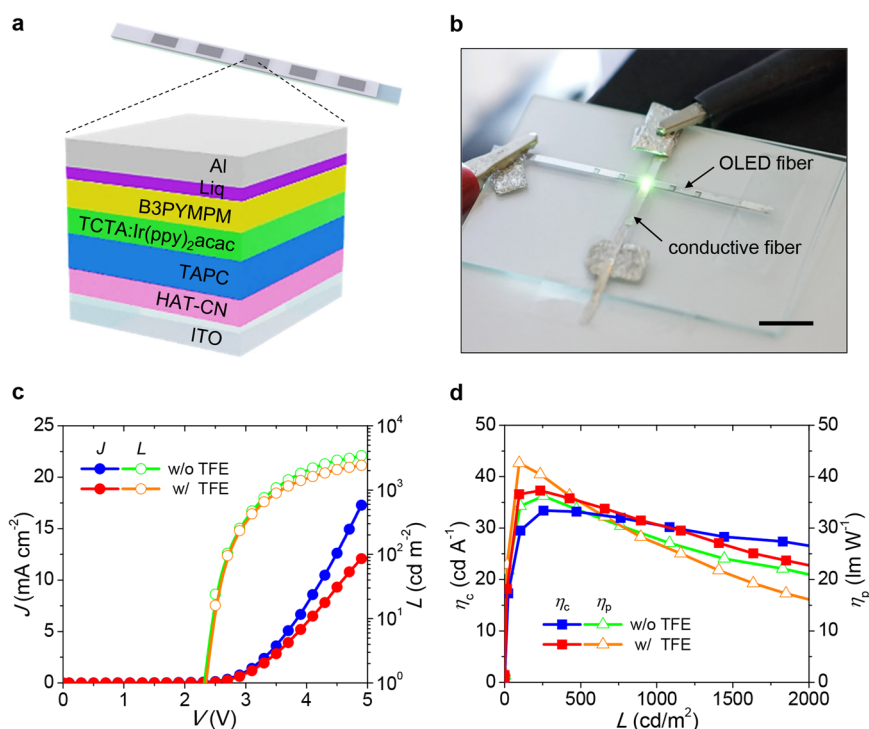


**Fig. 2** Electroluminescence performance of encapsulated OLED fiber pixels. **a** Schematic illustration of bottom-emission phosphorescent green OLED pixel structure. **b** Photograph of a fabricated OLED fiber orthogonally placed on a conductive fiber for operating its one pixel (scale bar: 1 cm). **c** Representative current density ( $J$ )-voltage ( $V$ )-luminance ( $L$ ) curves of OLED fiber pixels with and without TFEs. **d** Current efficiency ( $\eta_c$ ) and the power efficiency ( $\eta_p$ ) as a function of  $L$  for OLED fiber pixels corresponding to those in **c**.

on the rear side) as well as straightforward process handling<sup>19,32</sup>. The front side of as-prepared PI fibers was covered with a transparent multibarrier of 2-dyadic aluminum oxide ( $\text{Al}_2\text{O}_3$ , 30 nm)/parylene-C (500 nm)<sup>28,29</sup> by ALD and CVD, respectively, for the high-performance bottom encapsulation (water vapor transmission rate; WVTR =  $\sim 6 \times 10^{-5} \text{ g m}^{-2} \text{ day}^{-1}$ ). After deposition of the common conductor with a combination of indium tin oxide (ITO, 150 nm, conductivity;  $\sigma = \sim 10^4 \text{ S cm}^{-1}$ ) anode and chromium (Cr, 30 nm,  $\sigma = \sim 10^5 \text{ S cm}^{-1}$ ) conductive protector on this bottom TFE, a parylene-C separator (1  $\mu\text{m}$ ) with periodic apertures (area =  $1.5 \times 1.5 \text{ mm}^2$ , period = 6 mm) was produced through CVD and subsequent photolithographic dry etching for the OLED pixel definition. On the ITO anode exposed after wet-chemical etching of the Cr protector in these separator apertures, constituent layers of bottom-emission phosphorescent green OLEDs were thermally deposited, thereby creating a highly efficient but incompletely encapsulated OLED pixel array. Although given colored OLEDs were exploited herein for a proof of concept, other types of bottom-emission small-molecule OLEDs with different colors and materials combinations can be employed without any technical issues because of their similar deposition processes.

In contrast to the bottom encapsulation that was designed mainly for the high permeation barrier property, many additional factors need to be collectively considered in devising the top encapsulation of the interconnectable OLED fiber: The top encapsulation has to enable penetrable electrical flow for a link between each OLED pixel cathode and the contact pad placed on an outer fiber surface, robust protection of the damageable OLED materials from frictional abrasion at the fiber-to-fiber contacts, reduction in the mechanical stress applied to the OLED pixels, and enhancement of the instant contact reliability under the woven fiber configuration. To satisfy all requirements including the high permeation barrier, this study presents spatially manageable materials designs for the top encapsulation fabricated without any

wet-chemical processes that can significantly destroy the involving organic materials. The proposed top encapsulation system includes (i) dome-patterned polymer barrier (polyurethane; PU) for mechanical damage shielding, stress relaxation, and contact-area expansion, (ii) metal/oxide/polymer thin-film multibarrier (2-triad  $\text{Al}/\text{Al}_2\text{O}_3/\text{parylene-C}$ ) for oxygen/water permeation block, and (iii) partially constructed metal/oxide/metal multilayer anti-fuse ( $\text{Al}/\text{Al}_2\text{O}_3/\text{Al}/\text{Al}_2\text{O}_3/\text{Al}$ ) for electrical penetration. As a first step of the top encapsulation formation, Al (100 nm) base pads (area =  $1.5 \times 3.0 \text{ mm}^2$ ) were thermally deposited on the OLED pixel cathodes and their longitudinal vicinities to prepare lateral bypassing routes over the barrier insulators. Subsequently, the damage-protective pixel barrier of sturdy dome-shaped PU (area =  $2.0 \times 2.0 \text{ mm}^2$ , center thickness =  $\sim 100 \mu\text{m}$ ) that could offer favorable geometric effects (i.e., pixel stress reduction, contact reliability reinforcement) was fabricated through the procedures reported in our recent work<sup>19</sup>. The production of the domed PU barrier was followed by the implementation of the thin-film multibarrier comprising 2 triads of Al (100 nm)/ $\text{Al}_2\text{O}_3$  (5 nm)/parylene-C (1  $\mu\text{m}$ ) (i.e., metal/ultrathin oxide/polymer) deposited by thermal evaporation (with an area-defined shadow mask), ALD, and CVD, respectively. As with alternating dyads of oxide/polymer in the usual TFE multibarrier, this alternating triads system could offer the high permeation barrier property (WVTR =  $\sim 1 \times 10^{-4} \text{ g m}^{-2} \text{ day}^{-1}$  at 2 triads). This is due to suppressed permeation pinholes from the synergistic combination of Al and its ALD-processed oxide  $\text{Al}_2\text{O}_3$  and increased permeation paths by the intermediate parylene-C layer, which will be discussed more in the latter part. Meanwhile, the circumventing electrical path from the pixel cathode to the finally formed Al top contact pad (area =  $1.5 \times 3.0 \text{ mm}^2$ ) was achievable in this triads system without patterning the  $\text{Al}_2\text{O}_3$  insulator. When creating parylene-C via-holes on the edge areas of protruded Al pads by oxygen dry etcher, the  $\text{Al}/\text{Al}_2\text{O}_3/\text{Al}$  stack emerging here could serve as an electrical flow channel (Fig. 1b) because its

configuration corresponds to a dielectric antifuse<sup>33–35</sup> that can be a permanent conductor after the breakdown initiation. From the encapsulation point of view, the Al<sub>2</sub>O<sub>3</sub> layer typically has to be over a few tens of nanometer thickness for a reliable permeation block. By contrast, this system compels very thin Al<sub>2</sub>O<sub>3</sub> for the low-voltage antifuse initiation, considering the breakdown voltage ( $V_{BD}$ ) property linearly proportional to the dielectric thickness (e.g.,  $V_{BD} \sim 9.5$  V at 12-nm Al<sub>2</sub>O<sub>3</sub>)<sup>34,35</sup>. Since the high barrier performance could be attained only with a 5-nm thick Al<sub>2</sub>O<sub>3</sub> configuration, we could design the reasonably low-voltage antifuse ( $V_{BD} \sim 7.5$  V) with double Al<sub>2</sub>O<sub>3</sub> layers (i.e., Al/Al<sub>2</sub>O<sub>3</sub>/Al/Al<sub>2</sub>O<sub>3</sub>/Al) (This will also be discussed in more detail later.)

The fabrication of the encapsulated interconnectable OLED fibers was completed after the formation of the Cr (30 nm)/silver (Ag, 500 nm) addressing conductor on the rear fiber side for pixel driving by using thermal evaporation with an aperture-defined shadow mask. Figure 1c exhibits a representative photograph of the resulting OLED fiber, where the OLED pixels with upper contact pads can emit the light through the apertures existing in the bottom addressing conductor. Interlacing horizontal and vertical arrays of these OLED fibers (denoted as *x*-fibers and *y*-fibers) under the fiber-to-fiber contact layout resulted in a woven fiber matrix with the OLED pixels appearing at every cross-spots (Fig. 1d). As shown in Fig. 1e, a fabricated prototype of the woven fiber display consisting of 10 × 10 OLED fibers was successfully driven via the passive matrix scheme, in which the ITO/Cr common conductors on the front fiber sides and the Cr/Ag addressing conductors on the rear fiber sides were used as the data-lines and the scan-lines in the addressing process, respectively. More details of overall device fabrication procedures are available in the Supplementary Information (Supplementary Methods, Supplementary Fig. 4).

### Electroluminescence performance of OLED fibers

The EL characteristics of the proposed OLED fibers were experimentally examined to manifest the attainability of high-performance lighting fibers. Figure 2a depicts the tested OLED fiber pixel structure composed of ITO (150 nm) anode, 1,4,5,8,9,11-hexaazatriphenylene-hexacarbonitrile (HAT-CN, 5 nm) hole injection layer, 4,4'-cyclohexylidenebis[N,N-bis(4-methylphenyl) benzeneamine] (TAPC, 40 nm) hole transport layer, tris(4-carbazoyl-9-ylphenyl)amine:bis[2-(2-pyridinyl-N)phenyl-C](acetylacetonato)iridium(III) (TCTA:Ir(ppy)<sub>2</sub>(acac), 8 wt%, 25 nm) emitting layer, 4,6-bis(3,5-di(pyridine-3-yl)phenyl)-2-methylpyrimidine (B3PYMPM, 35 nm) electron transport layer, 8-hydroxyquinolinolato-lithium (Liq, 1 nm) electron injection layer, and Al (100 nm) cathode, which is an efficient phosphorescent green OLED confirmed on a PI plate (Supplementary Fig. 5). The representative current density (*J*)-voltage (*V*)-luminance (*L*) curves of the TFE-passivated (i.e., fully encapsulated) OLED fiber pixels, measured with the perpendicularly placed Cr/Ag conductive fiber (Fig. 2b), are presented in Fig. 2c, where those of the TFE-less OLED fiber pixels (i.e., only with the domed PU barrier and Al base/contact pads) are also displayed to clarify the performance variation evoked from the introduced TFEs. The TFE-passivated OLED pixels could be turned on at a low voltage level of ~2.3 V once the antifuse in the top TFE was activated. Since their luminance rapidly rose to a reasonably high level as increasing the applied voltage (~2400 cd m<sup>-2</sup> at 4.9 V), the high brightness could be achieved as in the OLED plate devices. Compared with the TFE-less OLED pixels (~3400 cd m<sup>-2</sup> at 4.9 V), diminished luminance was observed at the TFE-passivated OLED pixels. This resulted from increased series resistance arising from the inserted antifuse in the top TFE (~12 and ~17 mA cm<sup>-2</sup> at 4.9 V for the TFE-passivated and TFE-less pixels, respectively), not from any materials degradations during the TFE formation, as supported by their similar levels in the current efficiency ( $\eta_c \sim 35$  cd A<sup>-1</sup>) and the power efficiency ( $\eta_p \sim 40$  lm W<sup>-1</sup>) (Fig. 2d). It needs to be

mentioned that the relatively severe roll-off behavior of the TFE-passivated OLED pixels at high luminance values seems to be attributed to the suppressed heat dissipation property provoked by thermally insulating TFE sublayers<sup>36–38</sup>.

### Electrical properties of OLED fibers and driving characteristics of their textiles

To avert unexpected device damage at the first operation of as-fabricated OLED fibers with TFEs, the antifuse in the top TFE has to be activated at a moderately low voltage level that does not suddenly yield the intensified current over the device. For designing such low-voltage TFE antifuses, we preferentially measured  $V_{BD}$  levels of the antifuse samples consisting of Al/Al<sub>2</sub>O<sub>3</sub>/Al multistack with a fixed Al<sub>2</sub>O<sub>3</sub> thickness of 5 nm, as shown in Fig. 3a. As the number of Al<sub>2</sub>O<sub>3</sub> layers increased from 1 (i.e., Al/Al<sub>2</sub>O<sub>3</sub>/Al) to 3 (i.e., Al/Al<sub>2</sub>O<sub>3</sub>/Al/Al<sub>2</sub>O<sub>3</sub>/Al/Al<sub>2</sub>O<sub>3</sub>/Al), the  $V_{BD}$  monotonically escalated from ~4.9 to ~10.2 V due to the electrical connection of the antifuse in series. Although multiple Al<sub>2</sub>O<sub>3</sub> layers in the antifuse and thus multiple triadic barriers in the TFE can facilitate the permeation blocking property, their increased  $V_{BD}$  was apparently unfavorable to the device reliability. This observation means an empirical compromise needs to be involved in determining the Al<sub>2</sub>O<sub>3</sub> layer number of the TFE antifuse: The double Al<sub>2</sub>O<sub>3</sub> layers (i.e., Al/Al<sub>2</sub>O<sub>3</sub>/Al/Al<sub>2</sub>O<sub>3</sub>/Al) with a  $V_{BD}$  of ~7.3 V sounds reasonably acceptable in consideration of the EL parameters (~12,000 cd m<sup>-2</sup>, ~150 mA cm<sup>-2</sup>) of OLEDs in this voltage range. The OLED fibers passivated with the 2 triads multibarrier TFE can be safely stabilized after several voltage sweeps for the aging of the initiated antifuse, as indicated in Fig. 3b.

To explicate the driving characteristics of woven OLED fiber displays, Fig. 3c provides a schematic illustration of 8 × 8 OLED fiber arrays operated by the passive matrix addressing scheme. Here, the data-lines (ITO/Cr common conductors) and the scan-lines (Cr/Ag addressing conductors) of 8 *x*-fibers are denoted as  $d_{x1} \sim d_{x8}$  and  $s_{x1} \sim s_{x8}$ , and those of 8 *y*-fibers are  $d_{y1} \sim d_{y8}$  and  $s_{y1} \sim s_{y8}$ . As pixels on the *x*-fiber data-lines are linked to the *y*-fiber scan-lines, and likewise, pixels on the *y*-fiber data-lines are linked to the *x*-fiber scan-lines, the addressing for all cross-spot pixels is feasible in this woven fiber matrix. The fiber interconnections can be organized into four distinguishable data-lines/scan-lines combinations: odd-data/odd-scan and even-data/even-scan combinations for the *x*-fiber pixels (i.e., ( $d_{x1}, d_{x3}, d_{x5}, d_{x7}$ )/( $s_{y1}, s_{y3}, s_{y5}, s_{y7}$ ) and ( $d_{x2}, d_{x4}, d_{x6}, d_{x8}$ )/( $s_{y2}, s_{y4}, s_{y6}, s_{y8}$ )) and odd-data/even-scan and even-data/odd-scan combinations for the *y*-fiber pixels (i.e., ( $d_{y1}, d_{y3}, d_{y5}, d_{y7}$ )/( $s_{x2}, s_{x4}, s_{x6}, s_{x8}$ ) and ( $d_{y2}, d_{y4}, d_{y6}, d_{y8}$ )/( $s_{x1}, s_{x3}, s_{x5}, s_{x7}$ )). This implies that pixels selected from the different interconnection combinations can be controlled individually in the addressing process. For instance, 4 pixels at (3, 3), (4, 4), (4, 5), and (5, 6) cross-spots in the given illustration of Fig. 3c are simultaneously turned on by activated switch pairs of  $d_{x3}/s_{y3}$ ,  $d_{x4}/s_{y4}$ ,  $d_{y5}/s_{x4}$ , and  $d_{y6}/s_{x5}$ . By applying the passive matrix addressing scheme described above, an instance image representing 'sprout' could be successfully displayed on the experimental textile sample, as shown in the photograph in Fig. 3d.

### Long-term stability and deformability characteristics of OLED fibers

Due to the high-grade permeation barrier properties of the present TFE system, the encapsulated OLED fiber pixels could achieve long-term stability in ambient conditions. Particularly, their resistance function against moisture allowed the stable operation in water, as demonstrated in Fig. 4a and Supplementary Movie 1. To quantitatively identify the moisture barrier performance, we conducted the electrical calcium (Ca) test<sup>30,39,40</sup> (Supplementary Fig. 6) for multilayers featured as the bottom

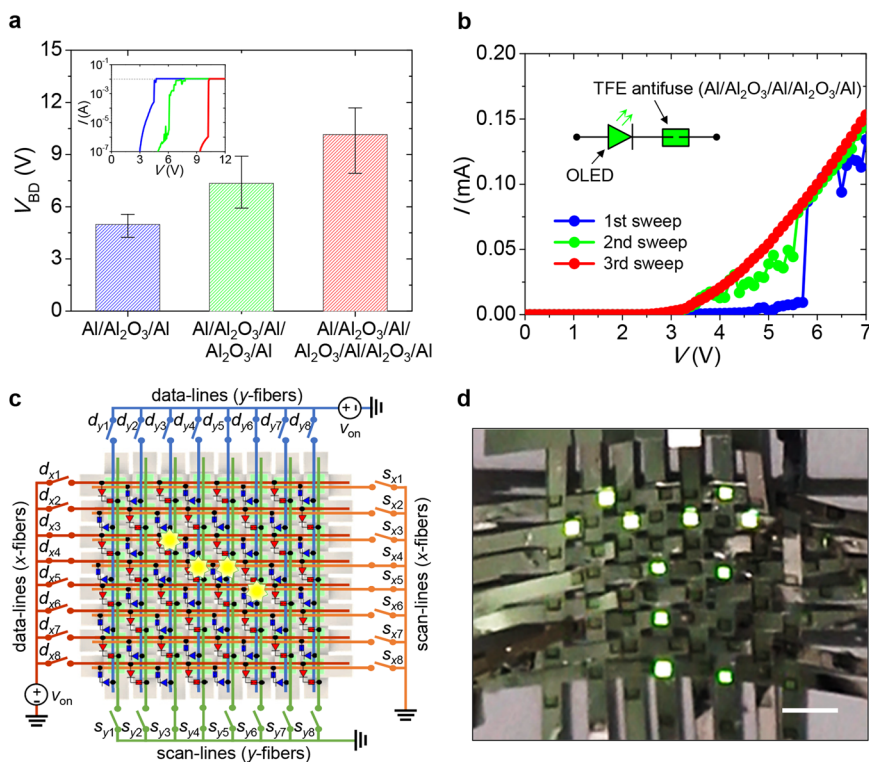


**Fig. 3** Electrical properties of encapsulated OLED fiber pixels and driving characteristics of woven OLED fiber displays. **a** Measured breakdown voltages ( $V_{BD}$ ) of 5-nm  $Al_2O_3$ -based dielectric antifuses comprising single (Al/ $Al_2O_3$ /Al), double (Al/ $Al_2O_3$ /Al/ $Al_2O_3$ /Al) or triple (i.e., Al/ $Al_2O_3$ /Al/ $Al_2O_3$ /Al/ $Al_2O_3$ /Al)  $Al_2O_3$  layers (error bar: standard deviation). The inset indicates representative breakdown current ( $I$ )-voltage ( $V$ ) curves of these antifuses in logarithmic scale. **b** Measured  $I$ - $V$  curves of an encapsulated OLED fiber pixel with the antifuse of double  $Al_2O_3$  layers for the first, second, and third voltage sweeps in the range of 0 ~ 7 V. **c** Illustration of the passive matrix addressing process for interlaced  $8 \times 8$  OLED fiber arrays, where the ITO/Cr data-lines ( $d_{x1} \sim d_{x8}$ ,  $d_{y1} \sim d_{y8}$ ) and the Cr/Ag scan-lines ( $s_{x1} \sim s_{x8}$ ,  $s_{y1} \sim s_{y8}$ ) of  $x$ - and  $y$ -fibers are linked to external voltage source ( $V_{on}$ ) and ground, respectively. Here, 8 individual switches ( $d_{x3}$ ,  $d_{x4}$ ,  $d_{y5}$ ,  $d_{y6}$ ,  $s_{x4}$ ,  $s_{x5}$ ,  $s_{y3}$ ,  $s_{y4}$ ) are activated for concurrently turning on 4 pixels at (3, 3), (4, 4), (4, 5), and (5, 6). **d** Photograph of the  $8 \times 8$  OLED fiber display operated by the passive matrix addressing method (scale bar: 5 mm).

and top TFEs at 30 °C and 90% relative humidity (RH), and derived their WVTR values. The dyadic  $Al_2O_3$ /polyethylene-C multilayers used as the bottom TFE presented substantially low WVTR levels ( $1.5 \times 10^{-4} \text{ g m}^{-2} \text{ day}^{-1}$  at 1 dyad,  $5.9 \times 10^{-5} \text{ g m}^{-2} \text{ day}^{-1}$  at 2 dyads, and  $4.7 \times 10^{-6} \text{ g m}^{-2} \text{ day}^{-1}$  at 3 dyads) (Supplementary Fig. 7) due to pinhole-less layers of the appropriately thick (30 nm)  $Al_2O_3$ , as reported in the literature<sup>18,27–29</sup>. By contrast, if the  $Al_2O_3$  thickness was limited to 5 nm as in the top TFE, the barrier function of such dyadic  $Al_2O_3$ /polyethylene-C multilayers did not work properly ( $1.5 \times 10^{-1} \text{ g m}^{-2} \text{ day}^{-1}$  at 1 dyad) because of its imperfect layer formation (Fig. 4b). Although the dyadic Al/polyethylene-C multilayers (i.e., Al instead of  $Al_2O_3$ ) did not have a good barrier property either, the triadic Al/ $Al_2O_3$ /polyethylene-C multilayers with both 100-nm Al and 5-nm  $Al_2O_3$  could exhibit the high barrier performance ( $7.0 \times 10^{-4} \text{ g m}^{-2} \text{ day}^{-1}$  at 1 triad and  $1.2 \times 10^{-4} \text{ g m}^{-2} \text{ day}^{-1}$  at 2 triads). This synergistic effect of Al/ $Al_2O_3$  is likely to be a consequence of suppressed Al surface pinholes by its oxide capping. A comparison of time-series luminance variations for the OLED fibers with and without the TFEs at a fixed current density ( $\sim 20 \text{ mA cm}^{-2}$ ) in Fig. 4c clearly supports the durability enhancement by the proposed fiber encapsulation system. Noticeable decay in ambient air (23 °C, 45% RH) and very rapid decay in deionized (DI) water (23 °C) were observed at the TFE-less OLED fibers (lifetime;  $\tau = \sim 5 \text{ h}$  in air,  $\sim 1 \text{ h}$  in water), whereas greatly mitigated and hence leveled decay in air and water could be monitored at the TFE-passivated OLED fibers ( $\tau = \sim 45 \text{ h}$  both in air and in water). In the meantime, the TFE-passivated OLED fibers could also obtain favorable mechanical stability due to the top encapsulation, including the  $\sim 100\text{-}\mu\text{m}$

thick domed PU barrier that alleviated the deformation stress applied to the pixels<sup>19</sup>. Fig. 4d evidently indicates negligible degradation of the OLED fiber performance after 100-cyclic bending deformation up to a bending radius of 1.5 mm. It is noteworthy that the proposed triadic TFE system can be more reliable in flexible operation than the typical TFE system owing to ductile Al and very thin fragile  $Al_2O_3$ .

## DISCUSSION

In summary, we demonstrated high-performance fibrous OLED textile displays that featured a large emission area and water resistance exceeding the reported textile devices. A matrix-addressable woven textile format consisting only of integrated interconnectable OLED fibers was implemented to substantiate the large emission area textiles. We designed decoupled fiber domains for a 1-dimensional array of phosphorescence OLED pixels with exclusive contacts and independent addressing conductor involved in the operation of interlaced other fibers. The long-term device durability was enabled by tailoring the encapsulation system to interconnectable OLED fiber pixels. In particular, the devised top TFE of 2-triadic Al/ultrathin  $Al_2O_3$ /polyethylene-C multilayer allowed not only the achievement of high permeation barrier property but also the construction of low-voltage dielectric antifuses that offered electrical circumventing channels between pixels and outer contact pads. The high EL performance and reliable bending stability of the OLED fibers were also successfully manifested, and the proof-of-concept

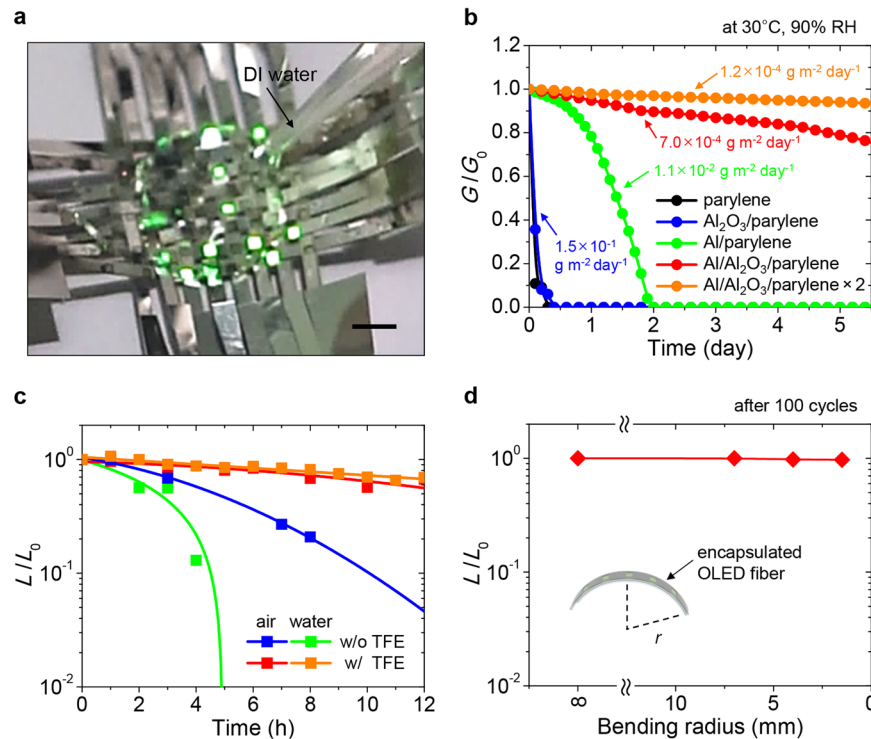


**Fig. 4** Stability and deformability characteristics of encapsulated OLED fibers. **a** Photograph of the operating OLED fiber display in a DI water drop (scale bar: 5 mm). **b** Normalized conductance ( $G/G_0$ ) of the electrical Ca test samples for parylene-C (1000 nm),  $Al_2O_3$ /parylene-C (5/1000 nm), Al/parylene-C (100/1000 nm), Al/ $Al_2O_3$ /parylene-C (100/5/1000 nm), and 2-set Al/ $Al_2O_3$ /parylene-C (100/5/1000/100/5/1000 nm) as a function of the storing time at 30 °C and 90% RH. The evaluated WVTR values of these samples are indicated for clarity. **c** Measured luminance ( $L$ ) normalized by the initial value ( $L_0$ ) for OLED fiber pixels with and without TFEs stored in ambient air (23 °C, 45% RH) and DI water (23 °C) as a function of the storing time at a fixed pixel current density of 20 mA/cm<sup>2</sup>. **d** Measured  $L$  variation normalized by the initial value ( $L_0$ ) for encapsulated OLED fiber pixels after 100 times bending repetition in accordance with various bending radii at a fixed pixel current density of 20 mA/cm<sup>2</sup>.

textiles of these fibers could be operated even in water through the passive matrix driving method tamed to the fiber network.

The device design concepts and fabrication strategies suggested in this study are readily applicable to related advanced classes of fibrous textile displays in several aspects. The scheme of defining decoupled fiber domains can be employed for single fiber integration of various lighting elements with addressing conductors for textile displays without addressing fibers (as in this work) or with other functional electronic elements/devices (e.g., sensors, energy harvesters) for multifunctional (or self-powered) textile displays. The presented passive matrix addressing for interlaced fiber networks may lead the device driving scheme in the early stage of fibrous textile displays before moving toward the active matrix textiles. The high-grade fiber TFEs with antifuses for interconnectable pixels and their wet-chemical-less fabrication process can be an up-and-coming solution for many vulnerable lighting fiber candidates (e.g., perovskite LEDs, polymer LEDs, quantum-dot LEDs) for being long-term stable fibrous textile displays.

## METHODS

### Fabrication of OLED fiber textiles

The device fabrication started with the preparation of rectangular PI fibers (width = 2 mm, height = 150  $\mu$ m, length = 70 mm) by cutting a PI plate through a programmable cutting machine (Cameo 3, Silhouette). On a PI fiber array attached to a polydimethylsiloxane (PDMS)-coated carrier glass, parylene-C (500 nm) and  $Al_2O_3$  (30 nm) were deposited by CVD (Lavida, Femto Science) with 150 ~ 160 °C powder vaporization temperature and by ALD (Lucida D100, NCD) with a trimethylaluminum (TMA) precursor (chamber temperature = 80 °C), respectively. After another set of parylene-C and  $Al_2O_3$  depositions for completing the 2-dyadic bottom TFE, ITO anode (150 nm, 110 °C annealing for 30 min) and Cr protector

(30 nm) were formed via sputter (KVT) and thermal evaporator (Sunic), respectively. A parylene-C separator (1  $\mu$ m) was deposited again through CVD, followed by photolithographic patterning (aperture area = 1.5  $\times$  1.5 mm<sup>2</sup>, aperture period = 6 mm) for the pixel definition by using oxygen reactive-ion etching ( $O_2$  RIE; Femto Science). The exposed Cr was wet-chemically etched (CR-7, Cyantek), after which OLED materials of HAT-CN (5 nm), TAPC (40 nm), TCTA:Ir(ppy)<sub>2</sub>(acac) (25 nm, 8 wt%), B3PYMPM (35 nm), Liq (1 nm), and Al (80 nm) were thermally deposited on ultraviolet-ozone (UVO)-treated ITO in alignment with a shadow mask. To form the top contact encapsulation, Al (100 nm) base pads (area = 1.5  $\times$  3.0 mm<sup>2</sup>) and  $MoO_3$  (50 nm) pre-barriers (area = 1.5  $\times$  1.5 mm<sup>2</sup>) were sequentially deposited first on the OLED pixel areas by thermal evaporation with dissimilar shadow masks. Subsequently, UV-curable PU (NOA 61, Norland) beforehand spin-coated on a UVO-treated PDMS featured stamp was transferred onto the pixels, and cured under UV light for producing the domed PU barriers. Next, Al (100 nm) pads (area = 1.5  $\times$  3.0 mm<sup>2</sup>),  $Al_2O_3$  (5 nm), and parylene-C (1  $\mu$ m) were deposited by thermal evaporation with a shadow mask, ALD (chamber temperature = 80 °C), and CVD, respectively, and thereafter, via-holes were created in the parylene-C by  $O_2$  RIE with a shadow mask. The 2-triadic top TFE with antifuse channels was done after repeating a set of Al pads/ $Al_2O_3$ /parylene-C depositions, via-hole patterning, and the final deposition of Al contact pads. For the formation of the periodically perforated (aperture area = 1.5  $\times$  1.5 mm<sup>2</sup>) addressing conductor on the opposite fiber side, Cr (30 nm) and Ag (500 nm) were deposited on the flipped array of processed PI fibers by thermal evaporation. The OLED fibers were eventually ready for weaving, and the interlacing proceeded to finalize the encapsulated OLED fiber textiles. The step-by-step fabrication protocols can be found in the Supplementary Methods.

### Electroluminescence characterizations and driving implementations

Measurements of the  $J$ - $V$ - $L$  curves and their  $\eta_c$  and  $\eta_b$  derivatives for the OLED fiber pixels were conducted using a set of the source meter (Series

2400, Keithley) and spectroradiometer (BM-7AS, Topcon). To execute the passive matrix driving of woven OLED fiber textiles, the common conductors and addressing conductors of fibers were connected to a programmable matrix switch module (U802) through line-patterned conductive films (Heat Seal Connectors, Elform).

### Permeation barrier characterizations

The WVTRs of thin-film barriers were assessed through the electrical Ca test that offered a characterization equation as<sup>30,39,40</sup>

$$\text{WVTR} = -n \frac{M_{\text{H}_2\text{O}}}{M_{\text{Ca}}} \delta_{\text{Ca}} \rho_{\text{Ca}} \frac{L}{W} \frac{dG}{dt}, \quad (1)$$

where  $n$ : molar equivalent (2 for water),  $M_{\text{H}_2\text{O}}/M_{\text{Ca}}$ : molar mass ratio of water to Ca,  $\delta_{\text{Ca}}$ : Ca density,  $\rho_{\text{Ca}}$ : Ca resistivity,  $L$ : pad length,  $W$ : pad width, and  $G$ : pad conductance. To prepare the Ca test sample, a 250-nm thick Ca pad ( $L = 15 \text{ mm}$ ,  $W = 10 \text{ mm}$ ) thermally deposited on the center of a glass plate ( $38 \times 25 \text{ mm}^2$ ) with Al lead contacts was sealed with the examining thin-film barrier on a 50- $\mu\text{m}$  thick polyethylene terephthalate (PET,  $25 \times 25 \text{ mm}^2$ ) and edge-embrocated UV-curable sealant (XNR 5570-Ba, Nagase) in a nitrogen-filled glove box. The conductance changes of the Ca test samples stored in a climate chamber set at 30 °C and 90% RH were monitored using an in-situ multimeter (Model 2750, Keithley).

### DATA AVAILABILITY

The data that support the findings of this study are available from the corresponding author upon reasonable request.

Received: 9 February 2022; Accepted: 15 July 2022;

Published online: 02 August 2022

### REFERENCES

- Zeng, W. et al. Fiber-based wearable electronics: A review of materials, fabrication, devices, and applications. *Adv. Mater.* **26**, 5310–5336 (2014).
- Yetisen, A. K. et al. Nanotechnology in textiles. *ACS Nano* **10**, 3042–3068 (2016).
- Zhang, M. C. et al. Printable smart pattern for multifunctional energy-management e-textile. *Matter* **1**, 168–179 (2019).
- Cho, S. H. et al. Plasmonically engineered textile polymer solar cells for high-performance, wearable photovoltaics. *ACS Appl. Mater. Interfaces* **11**, 20864–20872 (2019).
- Kwon, S. et al. Recent progress of fiber shaped lighting devices for smart display applications – a fibertronic perspective. *Adv. Mater.* **32**, 1903488 (2020).
- Zhang, Z. T. et al. Textile display for electronic and brain-interfaced communications. *Adv. Mater.* **30**, 1800323 (2018).
- Jeong, S. Y. et al. Foldable and washable textile-based OLEDs with a multifunctional near-room-temperature encapsulation layer for smart e-textiles. *npj Flex. Electron.* **5**, 15 (2021).
- Shi, X. et al. Large-area display textiles integrated with functional systems. *Nature* **591**, 240–245 (2021).
- Liang, G. J. et al. Coaxial-structured weavable and wearable electroluminescent fibers. *Adv. Electron. Mater.* **3**, 1700401 (2017).
- Yang, Z. L., Wang, W. W., Pan, J. & Ye, C. H. Alternating current electroluminescent devices with inorganic phosphors for deformable displays. *Cell Rep. Phys. Sci.* **1**, 100213 (2020).
- Yang, H. F., Lightner, C. R. & Dong, L. Light-emitting coaxial nanofibers. *ACS Nano* **6**, 622–628 (2012).
- Zhang, Z. T. et al. A colour-tunable, weavable fibre-shaped polymer light-emitting electrochemical cell. *Nat. Photonics* **9**, 233–238 (2015).
- Peng, H. S. et al. Electrochromatic carbon nanotube/polydiacetylene nanocomposite fibres. *Nat. Nanotechnol.* **4**, 738–741 (2009).
- Zhou, Y. et al. Multicolor electrochromic fibers with helix-patterned electrodes. *Adv. Electron. Mater.* **4**, 1800104 (2018).
- Liu, M. M. et al. Large-area all-textile pressure sensors for monitoring human motion and physiological signals. *Adv. Mater.* **29**, 1703700 (2017).
- Lee, H. E. et al. Wireless powered wearable micro light-emitting diodes. *Nano Energy* **55**, 454–462 (2019).
- Zysset, C., Munzenrieder, N., Kinkeldei, T., Cherenack, K. & Troster, G. Woven active-matrix display. *IEEE Trans. Electron Devices* **59**, 721–728 (2012).
- Lee, S. M., Kwon, J. H., Kwon, S. & Choi, K. C. A review of flexible OLEDs toward highly durable unusual displays. *IEEE Trans. Electron Devices* **64**, 1922–1931 (2017).

- Song, Y. J. et al. Fibertronic organic light-emitting diodes toward fully addressable, environmentally robust, wearable displays. *ACS Nano* **14**, 1133–1140 (2020).
- Kwon, S. et al. Weavable and highly efficient organic light-emitting fibers for wearable electronics: A scalable, low-temperature process. *Nano Lett.* **18**, 347–356 (2018).
- Hwang, Y. H. et al. Bright-multicolor, highly efficient, and addressable phosphorescent organic light-emitting fibers: Toward wearable textile information displays. *Adv. Funct. Mater.* **31**, 2009336 (2021).
- Hwang, Y. H. et al. High-performance and reliable white organic light-emitting fibers for truly wearable textile displays. *Adv. Sci.* **9**, 2104855 (2022).
- Kim, W. et al. Soft fabric-based flexible organic light-emitting diodes. *Org. Electron.* **14**, 3007–3013 (2013).
- Kim, W. et al. Reliable actual fabric-based organic light-emitting diodes: Toward a wearable display. *Adv. Electron. Mater.* **2**, 1600220 (2016).
- Choi, S. et al. Highly flexible and efficient fabric-based organic light-emitting devices for clothing-shaped wearable displays. *Sci. Rep.* **7**, 6424 (2017).
- Lu, Q. et al. A review on encapsulation technology from organic light emitting diodes to organic and perovskite solar cells. *Adv. Funct. Mater.* **31**, 2100151 (2021).
- Jeong, E. G., Kwon, J. H., Kang, K. S., Jeong, S. Y. & Choi, K. C. A review of highly reliable flexible encapsulation technologies towards rollable and foldable OLEDs. *J. Inf. Disp.* **21**, 19–32 (2020).
- Wu, J. et al. Efficient multi-barrier thin film encapsulation of OLED using alternating  $\text{Al}_2\text{O}_3$  and polymer layers. *RSC Adv.* **8**, 5721–5727 (2018).
- Keum, C. et al. A substrateless, flexible, and water-resistant organic light-emitting diode. *Nat. Commun.* **11**, 6250 (2020).
- Jeong, E. G., Jeon, Y., Cho, S. H. & Choi, K. C. Textile-based washable polymer solar cells for optoelectronic modules: Toward self-powered smart clothing. *Energy Environ. Sci.* **12**, 1878–1889 (2019).
- Elam, F. M. et al. Atmospheric pressure roll-to-roll plasma enhanced CVD of high quality silica-like bilayer encapsulation films. *Plasma Process. Polym.* **14**, e1600143 (2017).
- Cherenack, K., Zysset, C., Kinkeldei, T., Munzenrieder, N. & Troster, G. Woven electronic fibers with sensing and display functions for smart textiles. *Adv. Mater.* **22**, 5178–5182 (2010).
- Zhang, G., Hu, C., Yu, P., Chiang, S. & Hamdy, E. Metal-to-metal antifuses with very thin silicon dioxide films. *IEEE Electron Device Lett.* **15**, 310–312 (1994).
- Tian, M., Zhong, H. C., Li, L. & Wang, Z. G. A new high-kappa  $\text{Al}_2\text{O}_3$  based metal-insulator-metal antifuse. *Solid-State Electron.* **144**, 13–16 (2018).
- Li, W. T., McKenzie, D. R., McFall, W. D., Zhang, Q. C. & Wisniewski, W. Breakdown mechanism of  $\text{Al}_2\text{O}_3$  based metal-to-metal antifuses. *Solid-State Electron.* **44**, 1557–1562 (2000).
- Park, J., Ham, H. & Park, C. Heat transfer property of thin-film encapsulation for OLEDs. *Org. Electron.* **12**, 227–233 (2011).
- Li, Y., Xiong, Y. F., Yang, H. Z., Cao, K. & Chen, R. Thin film encapsulation for the organic light-emitting diodes display via atomic layer deposition. *J. Mater. Res.* **35**, 681–700 (2020).
- Murawski, C., Leo, K. & Gather, M. C. Efficiency roll-off in organic light-emitting diodes. *Adv. Mater.* **25**, 6801–6827 (2013).
- Paetzold, R., Winnacker, A., Henseler, D., Cesari, V. & Heuser, K. Permeation rate measurements by electrical analysis of calcium corrosion. *Rev. Sci. Instrum.* **74**, 5147–5150 (2003).
- Kang, K. S., Jeong, S. Y., Jeong, E. G. & Choi, K. C. Reliable high temperature, high humidity flexible thin film encapsulation using  $\text{Al}_2\text{O}_3/\text{MgO}$  nanolaminates for flexible OLEDs. *Nano Res.* **13**, 2716–2725 (2020).

### ACKNOWLEDGEMENTS

This work was supported in part by the National Research Foundation of Korea (NRF) funded by the Ministry of Science, ICT (Grant NRF-2022R1A5A7000765, NRF-2019R1C1C1008201, and NRF-2021M3H4A6A01048300), and in part by the Technology Innovation Program (20018379, Development of high-reliability light-emitting fiber-based woven wearable displays) funded by the Ministry of Trade, Industry & Energy (MOTIE).

### AUTHOR CONTRIBUTIONS

H.S. and Y.J.S. contributed equally to this work. S.-M.L. conceived the idea, designed the experiment, and prepared the manuscript. H.S., Y.J.S., J.H., S.Y., and H.-E.C. performed the device fabrication and measurements. H.S., Y.J.S., S.Y., and S.-M.L. conducted the device driving. K.S.K. implemented the barrier characterizations. J.-H.K. and S.-M.L. studied the emission area modeling. H.S., Y.J.S., and S.-M.L. analyzed the

experimental data, organized the manuscript contents, and contributed to the manuscript completion.

### COMPETING INTERESTS

The authors declare no competing interests.

### ADDITIONAL INFORMATION

**Supplementary information** The online version contains supplementary material available at <https://doi.org/10.1038/s41528-022-00199-z>.

**Correspondence** and requests for materials should be addressed to Sung-Min Lee.

**Reprints and permission information** is available at <http://www.nature.com/reprints>

**Publisher's note** Springer Nature remains neutral with regard to jurisdictional claims in published maps and institutional affiliations.



**Open Access** This article is licensed under a Creative Commons Attribution 4.0 International License, which permits use, sharing, adaptation, distribution and reproduction in any medium or format, as long as you give appropriate credit to the original author(s) and the source, provide a link to the Creative Commons license, and indicate if changes were made. The images or other third party material in this article are included in the article's Creative Commons license, unless indicated otherwise in a credit line to the material. If material is not included in the article's Creative Commons license and your intended use is not permitted by statutory regulation or exceeds the permitted use, you will need to obtain permission directly from the copyright holder. To view a copy of this license, visit <http://creativecommons.org/licenses/by/4.0/>.

© The Author(s) 2022